A Hybrid Electrochemical Multi-Particle Model for Li-ion Batteries

Journal of The
Electrochemical Society

A Hybrid Electrochemical Multi-Particle Model for Li-ion Batteries

To cite this article: Haider Adel Ali Ali *et al* 2024 *J. Electrochem. Soc.* **171** 110523

Journal of The Electrochemical Society, 2024 **171** 110523

A Hybrid Electrochemical Multi-Particle Model for Li-ion Batteries

Haider Adel Ali Ali,[1,2] Luc H. J. Raijmakers,[1,z] Hermann Tempel,[1] Dmitri L. Danilov,[1,3] Peter H. L. Notten,[1,3] and Rüdiger-A. Eichel[1,2]

[1]*Forschungszentrum Jülich GmbH, Institute of Energy Technologies (IET-1), 52428 Jülich, Germany*
[2]*RWTH Aachen University, Institute of Physical Chemistry, 52074 Aachen, Germany*
[3]*Eindhoven University of Technology, 5600 MB, Eindhoven, The Netherlands*

Physics-based models have proven to be effective tools for predicting the electrochemical behavior of Li-ion batteries. Among the various physics-based models, the Doyle-Fuller-Newman (DFN) model has emerged as the most widely employed. In response to certain limitations of the DFN model, the multiple particle-Doyle-Fuller-Newman (MP-DFN) model was introduced. The MP-DFN model utilizes multiple electrode particle sizes, addressing internal concentration heterogeneities and more realistically simulate diffusion processes in the electrodes. However, the model requires relatively high computational cost. This work introduces the Padé approximation for the MP-DFN model, resulting in the simplified MP-DFN model, leading to a faster simulation time. However, depending on battery design and operation conditions, this solution shows to have lower accuracy compared to the MP-DFN. To overcome these challenges, this study also introduces a hybrid MP-DFN model. This model uses a novel approach aimed at striking a balance between accuracy and computational speed. The hybrid MP-DFN model integrates both the finite difference method (FDM) and Padé approximation to effectively address the challenges posed by multiple particle sizes within the electrodes. The choice between FDM or the approximations for a specific particle in the electrode is determined by the scaled diffusion length.
 [DOI: 10.1149/1945-7111/ad92dd]

Manuscript submitted July 29, 2024; revised manuscript received October 2, 2024. Published November 26, 2024.

Supplementary material for this article is available online

Li-ion batteries (LIBs) are a promising solution for energy storage in both automotive applications and broader energy storage systems because of their exceptional energy and power densities.[1] Therefore, LIBs have permeated an expanding array of applications, spanning a broad range of scales to accommodate their diverse uses. This trend is clearly illustrated by the substantial increase in LIB sales with an eightfold growth rate from 2010 to 2018, reaching 160 GWh per year.[2] Projections suggest that annual LIB sales are expected to exceed up to 4 TWh by 2040.[3]

To improve LIB performance, design, and control, reliable battery models are essential. Physics-based electrochemical models, capable of accurately simulating and predicting LIB performance, serve as powerful tools for understanding battery behavior. The Dollye-Fuller-Newman (DFN) model[4,5] is a common example of a physics-based electrochemical model. The DFN model, derived from porous electrode theory, has been intensely used since its introduction in 1993 and remains a popular framework for LIB modelling to date.[6] The DFN model is composed of a set of partial differential equations (PDEs) that describe the electrochemical behavior of LIB, including ionic concentrations and potential within both the electrodes and liquid electrolyte.[6–8] When using the DFN model, it is common to neglect the heterogeneity of the electrode's microstructure, typically by simplifying all the electrode particles to the same size. This allows to reduce the complexity of the model and improves the simulation speed. However, in reality, electrode particles have different radii, leading to the presence of a particle size distribution.[9,10]

Various studies in the literature have implemented a particle size distribution into the DFN model, often referred to multiple particle-Doyle-Fuller-Newman (MP-DFN) model.[9,11–17] Kirk et al.[15] have shown that the traditional DFN model is unable to accurately predict LIB behavior in the low state-of-charge (SoC) region around the cut-off voltage. Implementing a particle size distribution in the DFN model led to a significant simulation accuracy improvement. In addition, the MP-DFN model has also shown high simulation accuracy for lithium iron phosphate (LFP) batteries.[13,16] However, although the MP-DFN has shown improved simulation accuracy with the implementation of distributed electrode particle sizes, increasing the number of particle radii also results in significantly longer simulation times.[15] Longer simulation times are undesirable because computational speed is crucial in tasks such as repetitive simulations or real-time state estimation. The computational burden in simulating the MP-DFN model arises from the application of Fick's second law of diffusion, often discretized spatially using the finite difference method (FDM).[18–22] In the MP-DFN model, this method must be applied to multiple particles with different radii, which does not hold for the traditional DFN model, where all particles are typically assumed to have the same size.

To reduce the computational burden of simulating diffusion inside the solid particles, various approximation methods, including polynomial approximation, Galerkin projection, and Padé approximation, have been proposed.[23–25] The latter method, which solves Fick's second law for solid particles using a rational function,[26–30] demonstrates relatively good accuracy across various conditions and reduces computing time compared to the traditional DFN model.[18,20,31,32] To the authors' best knowledge, Padé approximation for solving Fick's second law for solid particles has not been implemented in the MP-DFN model. Therefore, in this work, Padé approximation is introduced into the MP-DFN model, resulting in a simplified MP-DFN model, leading to faster computation times.

The trade-off between accuracy and computational speed is influenced by various factors, such as the diffusion constant inside the solid particle, the electrode particle size, and the applied C-rate. Addressing the challenge of balancing the accuracy of the MP-DFN model with the computational speed of the simplified MP-DFN model, as schematically illustrated in Fig. 1, can be achieved by incorporating both FDM and Padé approximation in a single model, resulting in the hybrid MP-DFN model. Both the hybrid MP-DFN model, and the simplified MP-DFN model, are introduced in this work.

The so-called scaled diffusion length (SDL), considering solid-state diffusion, particle size and C-rate, serves as an indicator to decide whether to apply the FDM or approximation for a specific particle in the electrode. This introduces a trade-off between simulation accuracy and computational speed, tailored to the desired

[z]E-mail: l.raijmakers@fz-juelich.de

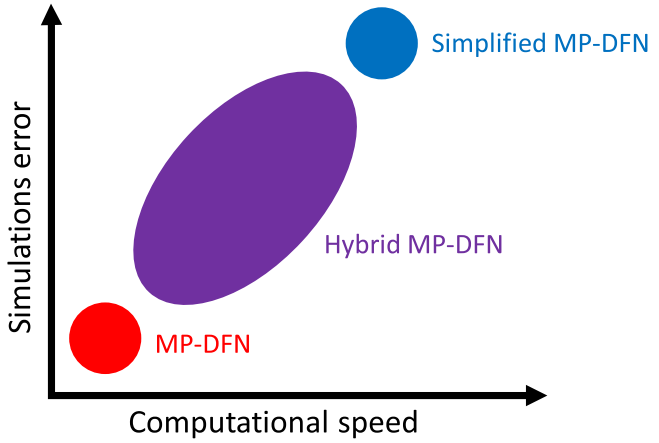

Figure 1. Schematic comparison of model simulation error and computational speed among the various models.

balance. In this study, the parameters of the MP-DFN model are mathematically optimized and validated with measurement data. Additionally, the simplified MP-DFN and hybrid MP-DFN models are applied and compared with the MP-DFN model, considering different SDL values. The comparison of various model performances was conducted under various operation conditions using key performance indicators (KPIs) focusing on accuracy and computational speed.

Model Development

Multiple-particle DFN model.—Figure 2 schematically illustrates the relation between a LIB and the (MP)-DFN model. Figure 2a shows the three macroscopic regions in the x-direction of a LIB: the porous negative electrode (neg) with thickness δ_{neg}, a porous separator (sep) with thickness δ_{sep} and the porous positive electrode (pos) with thickness δ_{pos}. These components add up to a total thickness L. Each electrode consists of a collection of microscopic solid particles, including active material, electrode

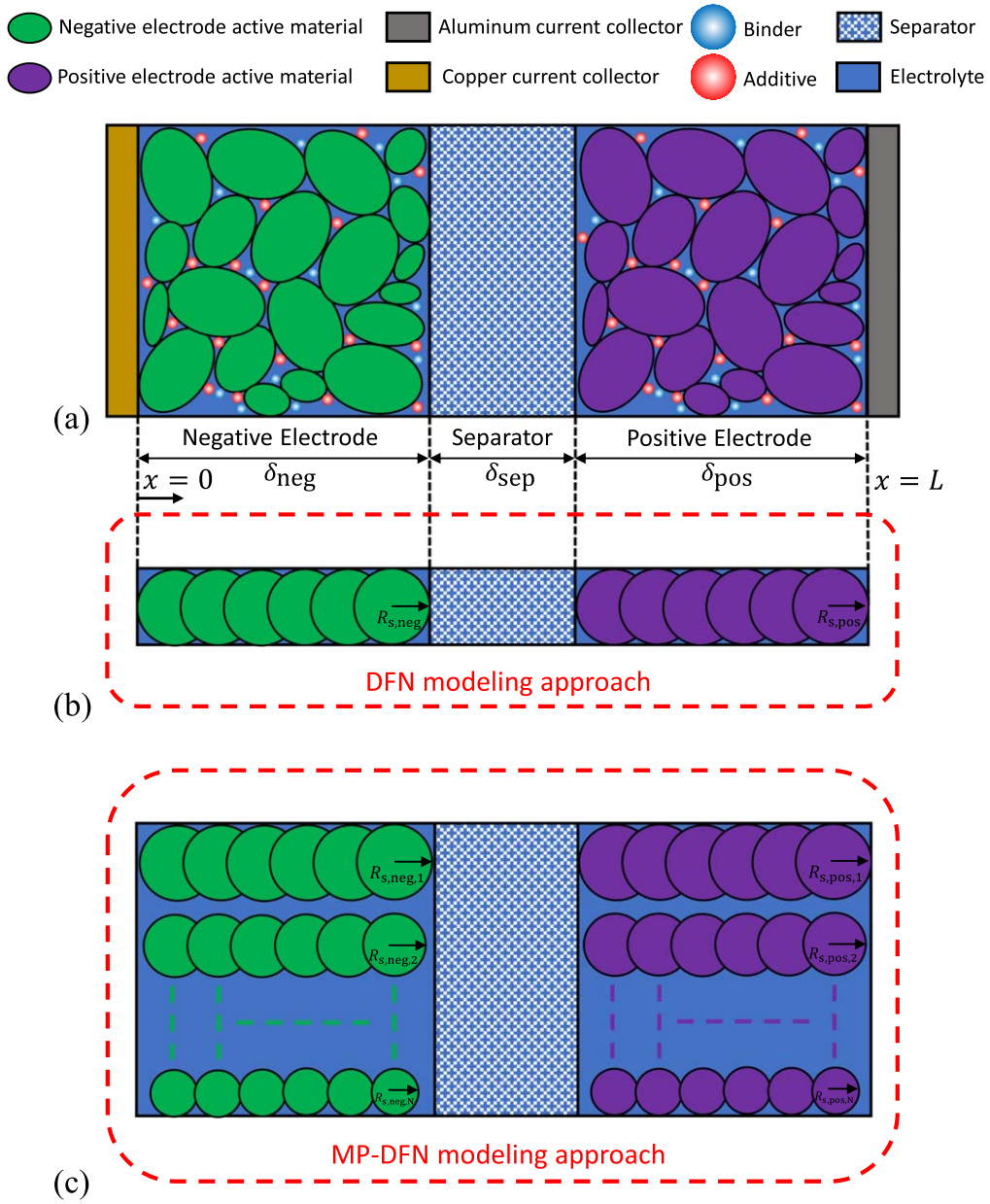

Figure 2. Schematic illustrations, within (a) the structure of a LIB and in (b) and (c) the active material and separator domains of the DFN and MP-DFN modeling approaches, respectively.

Table 1. Governing equations of the MP-DFN model.

Li-ions concentration in solid phase	$\frac{\partial c_{s,k}(r_k,t)}{\partial t} = \frac{D_s}{r_k^2}\frac{\partial}{\partial r_k}\left(r_k^2\frac{\partial c_{s,k}(r_k,t)}{\partial r_k}\right)$	(1a)
Boundary condition	$\frac{\partial c_{s,k}(r_k,t)}{\partial r_k}\Big\|_{r_k=0} = 0,\ -D_s\frac{\partial c_{s,k}(r_k,t)}{\partial r_k}\Big\|_{r_k=R_{s,k}} = j_{Li,k}(x,t)$,	(1b)
Li-ions concentration in the electrolyte phase	$\varepsilon_e\frac{\partial c_e(x,t)}{\partial t} = \frac{\partial}{\partial x}\left(D_e\varepsilon_e^b\frac{\partial c_e(x,t)}{\partial x}\right) + \sum a_{s,k}(1-t_+^0)j_{Li,k}(x,t)f_k$	(2a)
Boundary condition	$\frac{\partial c_e(x,t)}{\partial x}\Big\|_{x=0} = \frac{\partial c_e(x,t)}{\partial x}\Big\|_{x=L} = 0$	(2b)
Specific interfacial surface area	$a_{s,k} = \frac{3\varepsilon_s}{R_{s,k}}$	(2c)
Potential solid phase	$\frac{\partial}{\partial x}\left(\sigma_s\varepsilon_s\frac{\partial\phi_s(x,t)}{\partial x}\right) = \sum a_{s,k}Fj_{Li,k}(x,t)f_k$	(3a)
Boundary condition	$\sigma_s\varepsilon_s\frac{\partial\phi_s(x,t)}{\partial x}\Big\|_{x=0} = \sigma_s\varepsilon_s\frac{\partial\phi_s(x,t)}{\partial x}\Big\|_{x=L} = \frac{I_{app}(t)}{A_{surf}}$	
	$\frac{\partial\phi_s(x,t)}{\partial x}\Big\|_{x=\delta_{neg}} = \frac{\partial\phi_s(x,t)}{\partial x}\Big\|_{x=L-\delta_{pos}} = 0$	(3b)
Potential in electrolyte phase	$\frac{\partial}{\partial x}\left(\kappa_e\varepsilon_e^b\frac{\partial\phi_e(x,t)}{\partial x} + \kappa_e\varepsilon_e^b\nu\frac{2RT(t)}{F}\frac{\partial\ln c_e(x,t)}{\partial x}\right) = -\sum a_{s,k}Fj_{Li,k}(x,t)f_k$	(4a)
Boundary condition	$\frac{\partial\phi_e(x,t)}{\partial x}\Big\|_{x=0} = \phi_e(x,t)\|_{x=L} = 0$	(4b)
Butler-Volmer equation	$j_{Li,k}(x,t) = \frac{i_{0,k}(x,t)}{F}\left(\exp\left(\alpha_a\frac{F}{RT(t)}\eta_k(x,t)\right) - \exp\left(\alpha_c\frac{F}{RT(t)}\eta_k(x,t)\right)\right)$	(5a)
Electrode overpotential	$\eta_k(x,t) = \phi_s(x,t) - \phi_e(x,t) - U_k(x,t) - R_f j_{Li,k}F$	(5b)
Exchange current density	$i_{0,k}(x,t) = k_0(c_e(x,t))^{\alpha_a}(c_s^{max} - c_{s,k}^{surf}(x,t))^{\alpha_a}(c_{s,k}^{surf}(x,t))^{\alpha_c}$	(5c)
Battery output voltage	$V_{cell}(t) = \phi_s(L,t) - \phi_s(0,t) - \frac{R_{cc}}{A_{surf}}I_{app}(t)$	(6)

binder and additive, of which the latter two are neglected in the modelling approach. During (dis)charging, Li-ions move between the two electrodes and through the electrolyte. Consequently, electrons move through the active material, the battery current collector and through the outer circuit.

Figure 2b illustrates a schematic representation of the DFN modeling approach, in which a single particle size, typically the average particle size, is used, denoted as $R_{s,neg}$ and $R_{s,pos}$ for the negative and positive electrodes, respectively. Figure 2c schematically shows the concept of the MP-DFN model, depicting multiple particles of different radii arranged in the vertical direction. The MP-DFN model is based on the DFN model but is modified to account for a particle size distribution by using particles with different radii. Therefore, instead of using one average particle size with radius R_s, such as for the DFN model, the MP-DFN model uses a number of N particle radii, denoted as $R_{s,neg,k}$ for the negative and $R_{s,pos,k}$ for the positive electrode, where $k = 1{:}\,N$. The parameter N is user-selectable; however, its careful consideration is essential. Choosing an excessively high value for N may result in prolonged computation times, while opting for an excessively low value could compromise simulation accuracy. Note that if $N = 1$, the MP-DFN reduces to the DFN model.

The MP-DFN model is governed by four non-linear PDEs coupled with the Butler-Volmer equation. The model equations are summarized in Table I, with parameter definitions provided in the list of symbols. The set of PDEs includes Fick's second law of diffusion (Eq. 1), governing the concentration in the solid phase of the kth particle ($c_{s,k}$), and the solid phase potential (ϕ_s), calculated by Ohm's law, shown in Eq. 3. Both $c_{s,k}$ and ϕ_s are defined within the porous electrode region, i.e., for $x \in [0, \delta_{neg}] \cup [L - \delta_{pos}, L]$. The concentration ($c_e$) and potential ($\phi_e$) in the electrolyte are described in Eqs. 2 and 4, respectively, and are defined for $x \in [0, L]$. The specific interfacial surface area of the kth particle is calculated in Eq. 2c. These four PDEs are coupled via the Butler-Volmer equation in Eq. 5a, which is used to describe the electrochemical reaction at the electrode/electrolyte interface within the domain $x \in [0, \delta_{neg}] \cup [L - \delta_{pos}, L]$. Equations 5b-5c are used for calculating the electrode overpotential (η_k) and exchange current density ($i_{0,k}$) of the kth particle. The battery voltage (V_{cell}) is then calculated with Eq. 6.

Simplified multiple-particle DFN model.—The application of the Padé approach to all particles transforms the MP-DFN model into the simplified MP-DFN model. Padé approximation is used to calculate $c_{s,k}$ (Eq. 1). To replace the computationally intensive FDM, a third-order Padé approximation is applied as it offers an optimal balance between accuracy and computational speed in comparison to other orders.[30] The transfer functions for obtaining the average ($c_{s,k}^{avg}$) and surface ($c_{s,k}^{surf}$) concentration in the solid phase of the kth particle are defined by[29]

$$\frac{c_{s,k}^{avg}(x,s)}{j_{Li,k}(x,s)} = \frac{1}{(4/3)\pi R_{s,k}^3}\int_0^{R_{s,k}} c_{s,k}(r_k,t)(4\pi r_k^2\,dr_k) = -\frac{3}{a_{s,k}FR_{s,k}s}, \quad [7a]$$

and

$$\frac{c_{s,k}^{surf}(x,s)}{j_{Li,k}(x,s)} = \frac{\frac{3}{R_{s,k}} + \frac{4R_{s,k}}{11D_s}s + \frac{R_{s,k}^3}{165D_s^2}s^2}{s\left(1 + \frac{3R_{s,k}^2}{55D_s}s + \frac{R_{s,k}^4}{3465D_s^2}s^2\right)}, \quad [7b]$$

respectively. The meaning of all parameters in Eqs. 7a–7b are given in the list of symbols.

Hybrid multiple-particle DFN model.—The hybrid MP-DFN modelling approach can be described as a combination of both FDM and Padé approximations for solving $c_{s,k}$. However, determining which particles in the range $k = 1{:}\,N$ should be computed using FDM or Padé approximation can pose a challenge. To overcome this challenge, a modified version of the SDL[33] is applied, defined as

$$SDL_k = \frac{1}{R_{s,k}}\sqrt{4D_s\frac{3600}{\text{C-rate}}}, \quad [8]$$

where D_s is the diffusion constant of the solid phase and $R_{s,k}$ the particle radius of particle kth. The SDL is a unitless measure for describing the characteristic length scale of diffusion within an electrode particle and is used in this work to determine whether the FDM or Padé approximation for a specific particle in the electrode

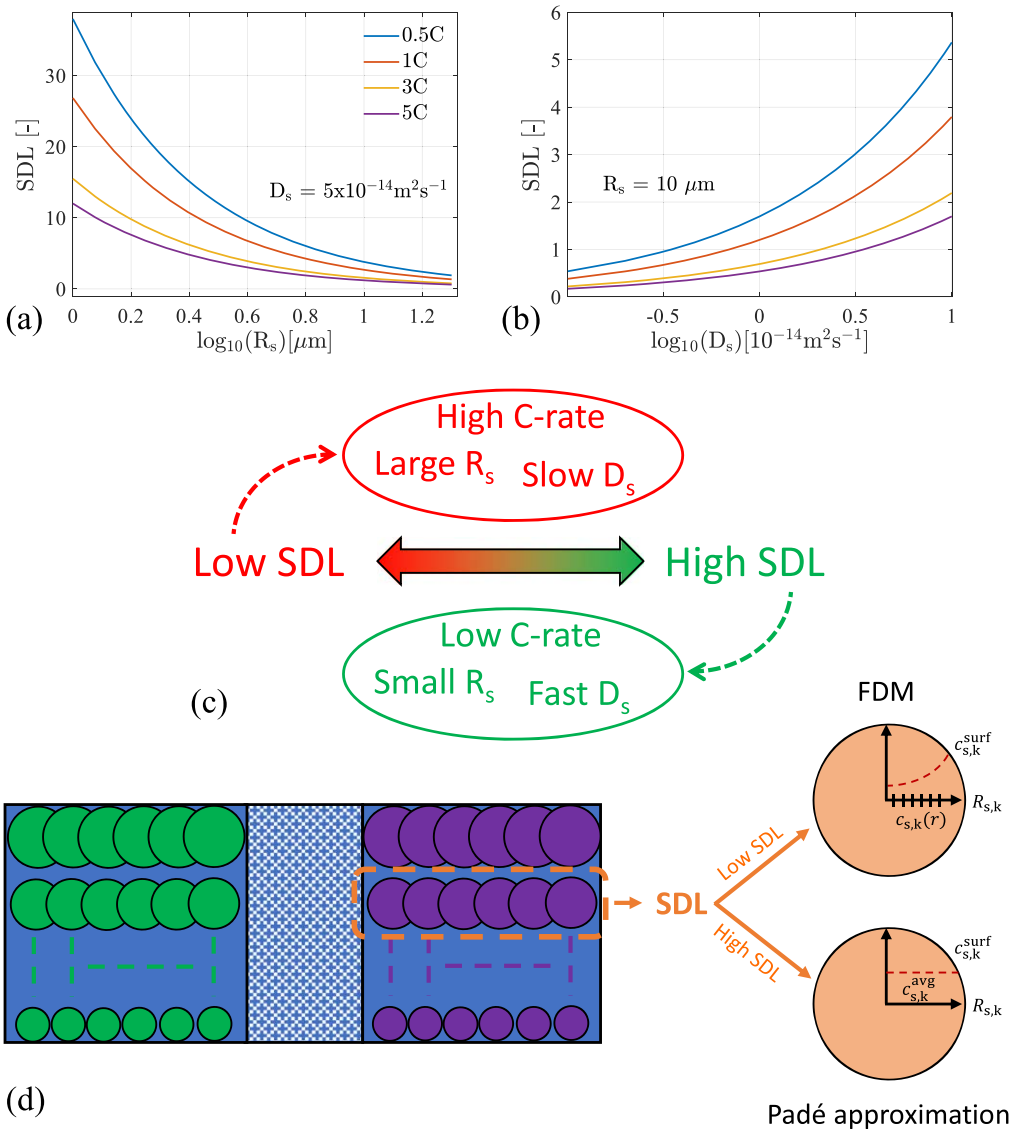

Figure 3. SDL as a function of the base-10 logarithm of particle size (a) and diffusion coefficient in the solid phase (b) for various C-rates. Schematic illustrations of high and low SDL (c), and the SDL serving as an indicator for choosing between FDM or Padé approximation for each particle (d).

should be applied. It is worth noting that the SDL excludes other parameters that are related to the electrode performance, such as film resistance (R_f), electrode thickness (δ), electrode surface area (A_{surf}), the active material volume fraction (ε_s), and overpotentials from the electrolyte dynamics.

Figures 3a–3b illustrates the results of simulations of the SDL (Eq. 8) under different scenarios. Figure 3a shows the SDL as a function of R_s at a 0.5, 1, 3, and 5 C-rate. D_s is kept constant at 5×10^{-14} m^2 s^{-1}. The results indicate that, across all C-rates, the SDL decreases with increasing values of R_s and that higher C-rates lead to lower SDL values. Figure 3b shows a scenario in which the SDL is calculated as a function of D_s. In this scenario, R_s is fixed at 10 μm. The simulations clearly demonstrate a reverse effect for D_s, showing that the SDL increases with increasing D_s for all C-rates. Furthermore, the lowest C-rate gives the highest SDL, as also concluded from Fig. 3a. The findings from the simulations in Figs. 3a–3b are schematically summarized in Fig. 3c.

The SDL can serve as an indicator of the strength of ionic concentration gradients in the particles. In cases with low SDL values, concentration gradients in particles may become pronounced, which may compromise the accuracy of Padé approximations. In such cases, the utilization of the FDM is recommended for accurate simulation results, as schematically shown in Fig. 3d. However, for high SDL values, concentration gradients are expected to be less pronounced. In such instances, the use of approximations does result in accuracies that are comparable to those of the FDM, but with reduced computational requirements.

The choice of the SDL value depends on the desired outcome of the simulation. If prioritizing accuracy over simulation speed is preferable, a high SDL value can be selected as a boundary to switch from FDM to approximation and the opposite can be done if simulation speed is prioritized over accuracy. However, selecting an SDL value to strike a balance between accuracy and simulation speed is not a straightforward process. This will be further discussed in Results and discussion section.

Model parameterization.—The MP-DFN model is parameterized and validated against experimental results adopted from Mohtat et al.,[11] of which the model parameters are shown in Table II. The model parameter set is based on the parametrization of a 5 Ah graphite/NMC pouch cell, fabricated at the University of Michigan Battery Lab. The experiments contain constant current (CC) charging data at four C-rates (0.2, 0.5, 1 and 2 C) from a fully discharged state (2.8 V) to a fully charged state (4.2 V). The model parameters

Table II. List of model parameters taken from Mohtat et al.[11].

Parameter	Negative electrode	Separator	Positive electrode	Unit
δ	62	12	67	μm
A_{surf}	0.205	—	0.205	m^2
ε_{s}	0.610	—	0.445	—
ε_{e}	0.3	0.4	0.3	—
$R_{\text{s,k}}$	[1.5, 2.0, 2.5, 3.0, 3.7]	—	3.5	μm
f_{k}	[0.10, 0.22, 0.30, 0.25, 0.13]	—	1	—
D_{s}	5.0×10^{-15}	—	8×10^{-15}	m^2s^{-1}
D_{e}	5.2×10^{-10}	5.2×10^{-10}	5.2×10^{-10}	m^2s^{-1}
σ_{s}	100		100	S m^{-1}
κ_{e}	1.3	1.3	1.3	S m^{-1}
b	1.5	1.5	1.5	—
t_+^0	0.38	0.38	0.38	—
k_0	1.1×10^{-11}		5.0×10^{-11}	$\text{mol}^{5/2}\text{m}^{-1/2}\text{s}^{-1}$
R_{f}	1×10^{-3}	—	0	$\Omega\,\text{m}^2$
R_{cc}	0	—	0	$\Omega\,\text{m}^2$
α	0.5	—	0.5	—
$c_{\text{s}}^{\text{max}}$	28746	—	35380	mol m^{-3}
$c_{\text{e}}^{\text{init}}$	1000	1000	1000	mol m^{-3}
$\chi_{100\%}$	0.8332	—	0.033	—
$\chi_{0\%}$	0.002	—	0.890	—
$U_{\text{neg}}(\chi) = 0.063 + 0.8\exp(-75(\chi + 0.001)) - 0.012\tanh\left(\frac{\chi-0.127}{0.016}\right) - 0.0118\tanh\left(\frac{\chi-0.155}{0.016}\right) - 0.0035\tanh\left(\frac{\chi-0.220}{0.020}\right)$ $- 0.0095\tanh\left(\frac{\chi-0.190}{0.013}\right) - 0.0145\tanh\left(\frac{\chi-0.490}{0.020}\right) - 0.08\tanh\left(\frac{\chi-1.030}{0.055}\right)$				V
$U_{\text{pos}}(\chi) = 4.3452 - 1.6518\chi + 1.6225\chi^2 - 2.0843\chi^3 + 3.5146\chi^4 - 2.2166\chi^5 - 0.5623 \times 10^{-4}\exp(109.451\chi - 100.006)$				V

from the reference study[11] were refitted, implementing additional particles in the negative electrode to increase particle radius non-uniformity. In particular, five particles are used in the positive electrode, while three particles are used in the negative electrode, as compared to the values reported in the reference study.[11] Another distinction with respect to the reference study arises from the use of the extended electrolyte single particle model (ESPM), which is a reduced-order model. The ESPM model from the reference study has the multiple particle feature implemented. For the MP-DFN model in this study, the value for the solid phase electronic conductivity (σ_{s}) was added from Ref. 18. For model parameter optimization, the function *fminsearchbnd*[34] in MATLAB is used. The root mean squared error (RMSE) served as an evaluation metric across all C-rates. A set of fitting parameters θ was defined, where θ includes D_{s}, $R_{\text{s,k}}$, f_{k} and k_0 for both electrodes. The objective function for m number of C-rates is therefore defined as

$$\hat{\theta} = \underset{\theta}{\text{argmin}} \sum_{i=1}^{m} \text{RMSE}_i(\theta), \qquad [9]$$

where $\hat{\theta}$ is the optimized set of parameters.

Model implementation.—Spatial and temporal discretization methods were applied to solve the PDEs described in Eqs. 1-4. The FDM or Padé approximation is used to discretize Eq. 1 along the r-direction for the MP-DFN, simplified MP-DFN and hybrid MP-DFN models. For Eqs. 2-4, the finite volume method (FVM) is applied, using the harmonic mean to determine boundary values between neighboring control volumes.[18] The resulting system of differential-algebraic equations was effectively solved using Newton's method,[19,21] with a tolerance set to 1×10^{-3} for all simulations. The simulation time-step was set to 1 s and the model temperature was set to isothermal conditions of 25 °C. It is important to note that isothermal conditions do not fully represent the behavior observed in the real world. Temperature variations can significantly influence battery performance, affecting parameters such as the reaction-rate constant, ionic conductivity, and diffusion coefficients in the solid and electrolyte phases.[35] Model programming and simulations were performed using MATLAB R2023a. A computer with AMD Ryzen 7 5700U CPU @ 1.8 GHz, 24 GB RAM and Windows operating system has been used.

All simulations initially start from a fully discharged condition of the cell at 2.8 V. Subsequently, a CC-charge was applied at 0.5, 1, 3, and 5 C, followed by a dynamic current profile in the form of the worldwide harmonized light vehicles test procedure (WLTP) with a discharge mean of 0.5 C. Figure 4 shows an example of such a load profile, starting with charging at 1 C, followed by the WLTP cycle.

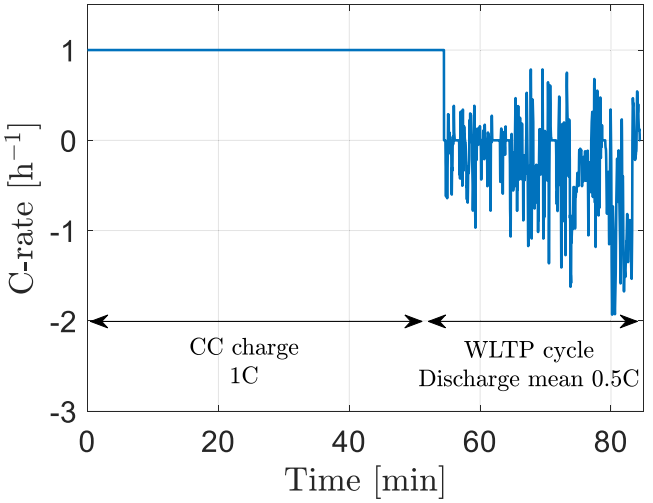

Figure 4. Example of the used load profile, with here a CC charge at 1 C followed by the WLTP cycle.

Table III. Optimized number of nodes for various operating conditions.

Charging C-rate	Negative electrode	Positive electrode	Separator	Negative particle	Positive particle
0.5	7	7	6	45	37
1	9	9	6	57	40
3	14	13	6	68	45
5	17	15	6	69	47

Table IV. Reference study and reoptimized MP-DFN model parameters.

Parameter	From Ref. 11	Optimized in this work	Difference [%]	Unit
$D_{s,neg}$	5×10^{-15}	7×10^{-15}	40	m^2s^{-1}
$D_{s,pos}$	8×10^{-15}	1×10^{-14}	25	m^2s^{-1}
$R_{s,neg,k}$	[1.5, 2.0, 2.5, 3.0, 3.7]	[1.2, 1.7, 2.5, 3.3, 4.1]	[20, 15, 0, 10, 11]	μm
$R_{s,pos,k}$	3.5	[1.9, 3.3, 4.9]	—	μm
$f_{k,neg}$	[0.10, 0.22, 0.30, 0.25, 0.13]	[0.11, 0.31, 0.21, 0.22, 0.15]	[10, 41, 30, 12, 15]	—
$f_{k,pos}$	1	[0.35, 0.31, 0.34]	—	—
$k_{0,neg}$	1.1×10^{-11}	8.2×10^{-12}	26	$mol^{5/2}m^{-1/2}s^{-1}$
$k_{0,pos}$	5.2×10^{-11}	3.3×10^{-11}	37	$mol^{5/2}m^{-1/2}s^{-1}$

Involving relatively high C-rates for CC charging, such as 3 and 5 C, allows the model to be evaluated under fast-charging conditions. Under these conditions, insufficient accuracy can lead to safety issues by, for example, underestimating the voltage of the negative electrode, potentially resulting in lithium plating.

To establish a valid model comparison and achieve optimal simulation accuracy and simulation speed, node optimization was performed. This process involved determining the appropriate number of discretized points along the r and x-directions. Nodes were evenly distributed across five grids: positive and negative electrode particles (r-direction), positive and negative electrode, and electrolyte (x-direction). Using a sufficient number of nodes ensures good accuracy, but an excessively large number increases computation time without a significant accuracy boost. Node optimization was performed by initially simulating the MP-DFN model with 80 nodes for each FDM and FVM grid at four C-rates (0.5, 1, 3, and 5 C). This simulation served as a reference simulation, as a higher number of nodes does not improve accuracy. Subsequently, the number of nodes was varied from 6 to 80, comparing the RMSE to a tolerance of 30 μV. The smallest number of nodes meeting the tolerance was selected and applied. The optimized number of nodes for the MP-DFN model was then applied to the simplified models. The optimized number of nodes at various operation conditions are shown in Table III.

To evaluate the computational speed of the various simplified models, the magnitude of simulation speed (MSS) is used, which can be calculated with

$$\text{MSS} = \left(\frac{t_f - t_s}{t_f} \right) \times 100, \qquad [10]$$

where t_f is the simulation time of the reference model (MP-DFN) and t_s is the simulation time of the simplified models, i.e., the hybrid MP-DFN and simplified MP-DNF models. All simulation times have been obtained by averaging the duration of 10 simulation repetitions, with the simulation time measured without pre-allocation of variables.

Results and Discussion

Parameter optimization of the MP-DFN model.—The introduction of additional particles into the electrode necessitates re-optimizing of certain model parameters to achieve an optimal fit of the MP-DFN model simulations to the experimental voltage profiles from Ref. 11. The parameters to be re-optimized are $R_{s,k}$ and f_k, but also D_s and k_0 for both electrodes to improve the accuracy. Table IV shows the optimized parameter results, the original parameter values, and the percentage differences. The key differences are a 40% and 25% change for $D_{s,neg}$ and $D_{s,pos}$, respectively. For $R_{s,neg,k}$, the difference ranges from 0% to 20%, while the difference for $f_{k,neg}$ ranges from 10% to 41%. Due to the increased number of particles in the positive electrode from one to three, the differences for $R_{s,pos,k}$ and $f_{k,pos}$ cannot be quantified. Furthermore, the parameters $k_{0,neg}$ and $k_{0,pos}$ show differences of 26% and 37% with respect to their original values, respectively. Although the percentage differences may appear significant, these values are within an acceptable range for diffusion coefficients and kinetic rate constants and are not considered excessively high.

Figure 5a shows the experimental (symbols) and simulated (lines) voltage charge profiles as a function of capacity for the four C-rates. Both the simulations with the original parameter set (blue lines) and the simulations with the reoptimized parameter set (dashed red lines) are shown. The differences between the simulations and experiments are shown in Figs. 5b–5e for all four C-rates. Obviously, the MP-DFN model with the reoptimized parameter set shows higher accuracy compared to the model with the parameter set from the reference study. Figure 5f shows the RMSE for each simulated C-rate for the reference and reoptimized parameter set. Improvements of 17% at 0.2 C, 27% at 0.5 C, 31% at 1 C, and 49% at 2 C are reached with respect to the original model parameter set. These findings conclusively demonstrate that the incorporation of additional particle sizes in the model and the use of the MP-DFN model led to improved simulation accuracy.

Model comparison.—Using the reoptimized parameter set from Parameter optimization of the MP-DFN model section and the load profile from Model implementation section, simulations are performed to compare the performance of the simplified MP-DFN and hybrid MP-DFN models with that of the MP-DFN model at different C-rates and SDLs. Figures 6a–6c shows the RMSE, maximum error, and MSS results as a function of SDL at various C-rates, where the MP-DFN model is used as a reference. Note that the y-axes values are calculated using the base-10 logarithm for fitting the linear regression lines. The regression lines are for further analysis and discussed later in this section. In each plot, each circular symbol represents a distinct particle radius. The negative electrode features

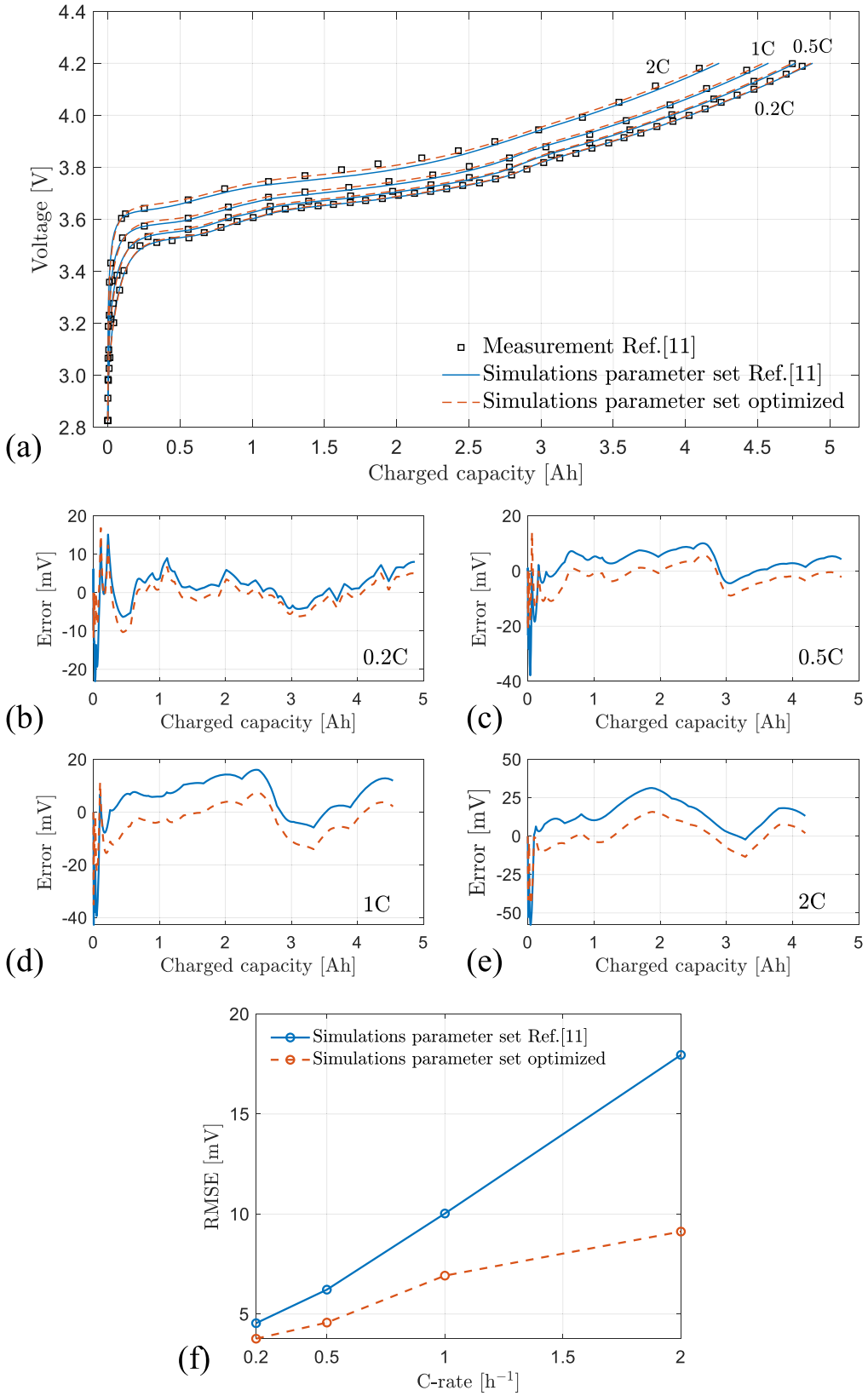

Figure 5. Comparison between the reference and reoptimized MP-DFN model simulations. Experiments and simulation results of the MP-DFN model during charging (a); the error between the simulation results and experiments at 0.2 C (b), 0.5 C (c), 1 C (d), 2 C (e); the RMSE of the error at the simulated C-rates (f). The blue lines show the results with parameters from the reference study[11] and the dashed red line the results with reoptimized parameters from this study.

five distinct particle radii, while the positive electrode has three, totaling eight particles represented by the eight symbols. In Table V, these eight particles are ranked as a function of SDL for each C-rate. Recall that the SDL is dependent on the C-rate and particle radius (Eq. 8). A low rank corresponds to a low SDL, and a high rank corresponds to a high SDL. When selecting no rank, Eq. 1a in the

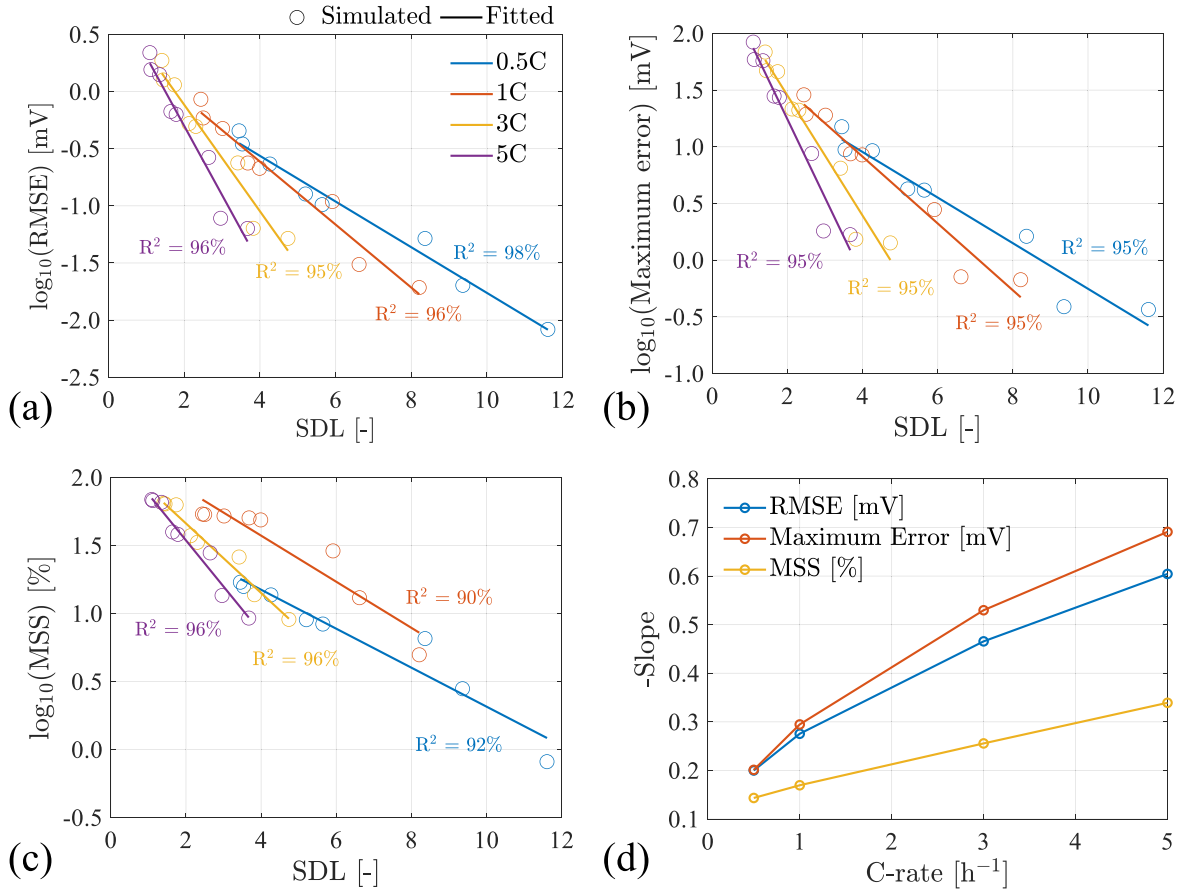

Figure 6. Simulation results (symbols) from the simplified MP-DFN and hybrid MP-DFN models compared to the MP-DFN reference model, with RMSE (a), maximum error (b), and MSS (c) as a function of SDL for four different C-rates. Linear regression lines are indicated by the lines. Slopes of the linear regression lines as a function of C-rate (d). Note that the y-axes values of (a)-(c) are calculated using the base-10 logarithm.

MP-DFN model is calculated for all particles with FDM, i.e., no approximation. This leads to a high simulation accuracy but to a low simulation speed. Choosing the SDL for the highest rank (i.e., 8) forces one particle to be calculated by Padé approximations and all other ones by FDM, turning the MP-DFN model into the hybrid MP-DFN model. Decreasing the rank can be continued until the lowest rank (i.e., 1) and lowest SDL, forcing all particles to be calculated by Padé approximations, resulting in the use of the simplified MP-DFN model. This leads to achieving the highest simulation speed, but also the lowest simulation accuracy. It is advised to adopt the SDL belonging to the highest applied C-rate. However, in some situations, the highest C-rate is applied only in short pulses, which is insufficient to generate high ionic concentration gradients in the particles. It is then unnecessary to calculate the SDL for the highest C-rate, which would otherwise require using FDM for many particles, resulting in slower simulations. In such cases, it is important to select the appropriate C-rate for calculating the SDL, considering both the C-rate and the duration of the pulse.

The results in Figs. 6a–6c demonstrate that the RMSE, maximum error, and MSS decrease as a function of SDL for the various C-rates. This is expected because with increasing SDL fewer approximations are used. The results also show that when operating at a low C-rate (e.g., 0.5 C), the difference between the MP-DFN and simplified MP-DFN model simulations is relatively small with an RMSE of 0.45 mV and a maximum error of 15 mV. However, at a high C-rate (e.g., 5 C), the difference becomes significant, with the simplified MP-DFN model reaching a high MSS, but also high errors, with RMSE values of 2.2 mV and a maximum error of 83.9 mV. Figure S1a-c shows the original values without base-10 logarithmic transformation for easier interpretation. The simulations demonstrate that the simplified MP-DFN model, which uses Padé approximation for all particles, do not provide accurate results for high C-rates, as the concentration inside the particles becomes more nonlinear. Therefore, the hybrid MP-DFN model allows for a trade-off between accuracy and computational speed, enabling a balance according to requirements of the model user.

The results in Figs. 6a–6c demonstrate that RMSE, maximum error, and MSS are close to a linear behavior if the results are calculated on a base-10 logarithm and plotted as such on the *y*-axis. Therefore, linear regression lines are fitted for all C-rates. The linear fit is strong, with the coefficient of determination (R^2) averaging 95%. For further analysis, the slopes of the linear regression lines are calculated and shown in Fig. 6d as a function of C-rate. It can be observed that the slopes show a non-linear growth; however, the growth for MSS is smaller in comparison. A high negative slope indicates that the regression line falls sharply as a function of SDL, reflecting a large difference between minimum and maximum

Table V. Particle ranking in ascending order based on SDL at various C-rates.

Rank	Electrode	$R_{s,k}$ [μm]	SDL (0.5 C)	SDL (1 C)	SDL (3 C)	SDL (5 C)
1	Negative	4.1	3.45	2.44	1.41	1.09
2	Positive	4.9	3.53	2.5	1.44	1.12
3	Negative	3.3	4.26	3.01	1.74	1.35
4	Positive	3.3	5.2	3.68	2.12	1.65
5	Negative	2.5	5.64	3.99	2.3	1.78
6	Negative	1.7	8.36	5.91	3.41	2.64
7	Positive	1.9	9.36	6.62	3.82	2.96
8	Negative	1.2	11.61	8.21	4.74	3.67

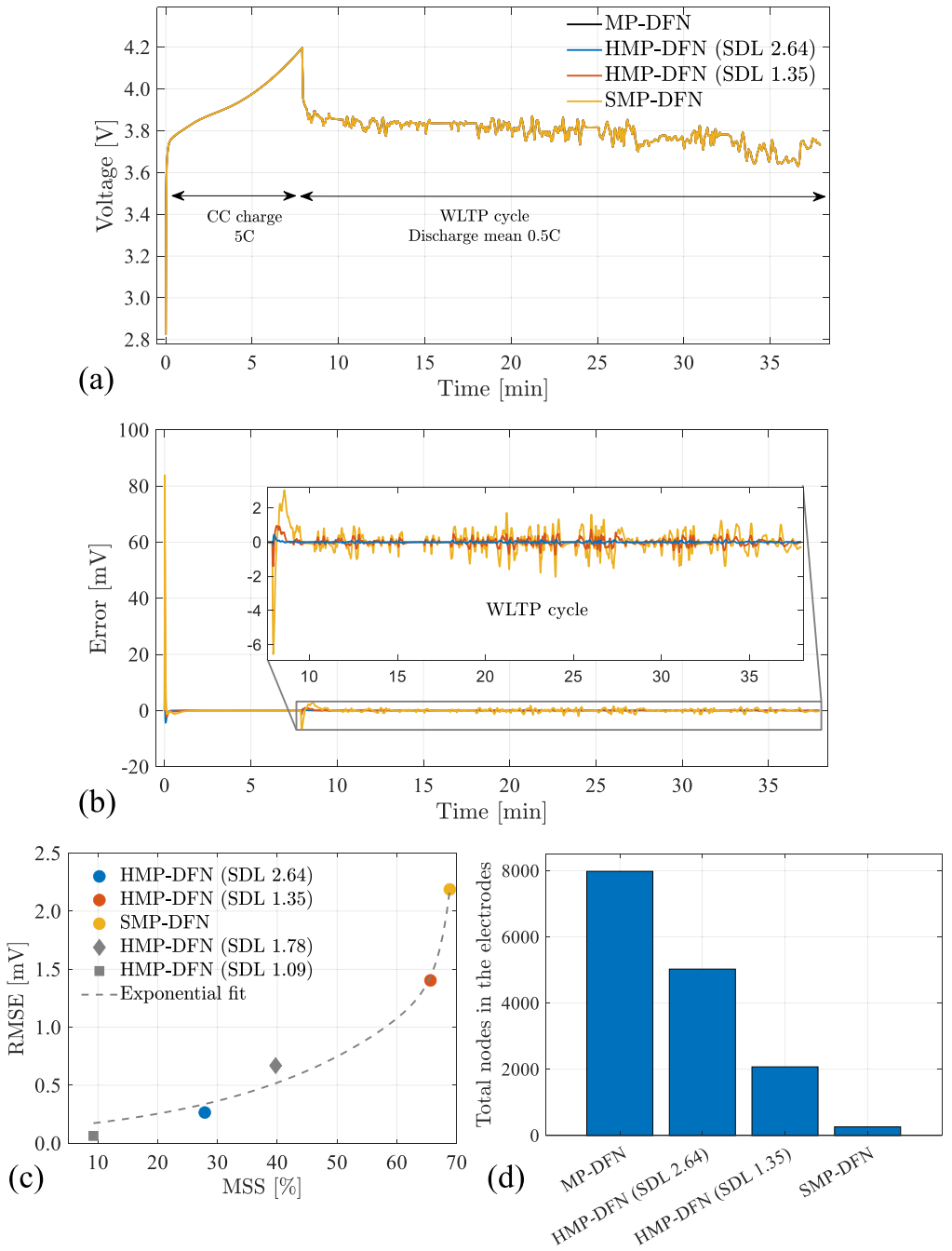

Figure 7. Comparison between the reference MP-DFN model, the hybrid (H)MP-DFN model using an SDL of 2.64 and 1.35, and the simplified (S)MP-DFN model. Simulated voltage curves (a), the error between the reference model and approximations (b), comparison between RMSE and MSS (c), and the total number of nodes in the electrodes for the various models (d).

RMSE, maximum error, and MSS. The slope is shown to be the highest for maximum error, followed by RMSE and MSS. The main reason for the differences in slope for the various C-rates is that the range between the highest and lowest SDL is dependent on the C-rate. For example, the SDL difference for 0.5 C is 8.16, resulting in a low slope, while for 5 C the SDL difference is 2.58, leading to a high slope (Table V). Particle radius and diffusion coefficient would also influence the slope but are more design-specific or change as a function of other conditions, such as temperature. Therefore, a sensitivity analysis in which these two parameters are evaluated is performed in Sensitivity analysis section.

The determination of the optimal SDL value is a nontrivial process, as it necessitates the establishment of a balance between accuracy and computational speed. Figure 7a shows simulation results with the load profile described in Model implementation section used as input. In this case, 5 C-rate CC-charging is applied followed by the WLTP. In total, four simulations are performed: a simulation with the MP-DFN model (black line), two simulations with the hybrid MP-DFN model using an SDL of 2.64 (blue line) and 1.35 (red line), and a simulation with the simplified MP-DFN model (yellow line). The MP-DFN model uses FDM for all particles and the simplified MP-DFN model uses Padé approximations for all particles with SDL 1.09. The hybrid MP-DFN model with an SDL of 2.64 uses Padé approximation for three particles and the hybrid MP-DFN model with an SDL of 1.35 uses Padé approximation for six particles. This can be taken from the "SDL (5 C)" column in Table V.

In terms of error, as shown in Fig. 7b, the results reveal an RMSE of 0.27 mV and 1.4 mV when using the hybrid MP-DFN model with

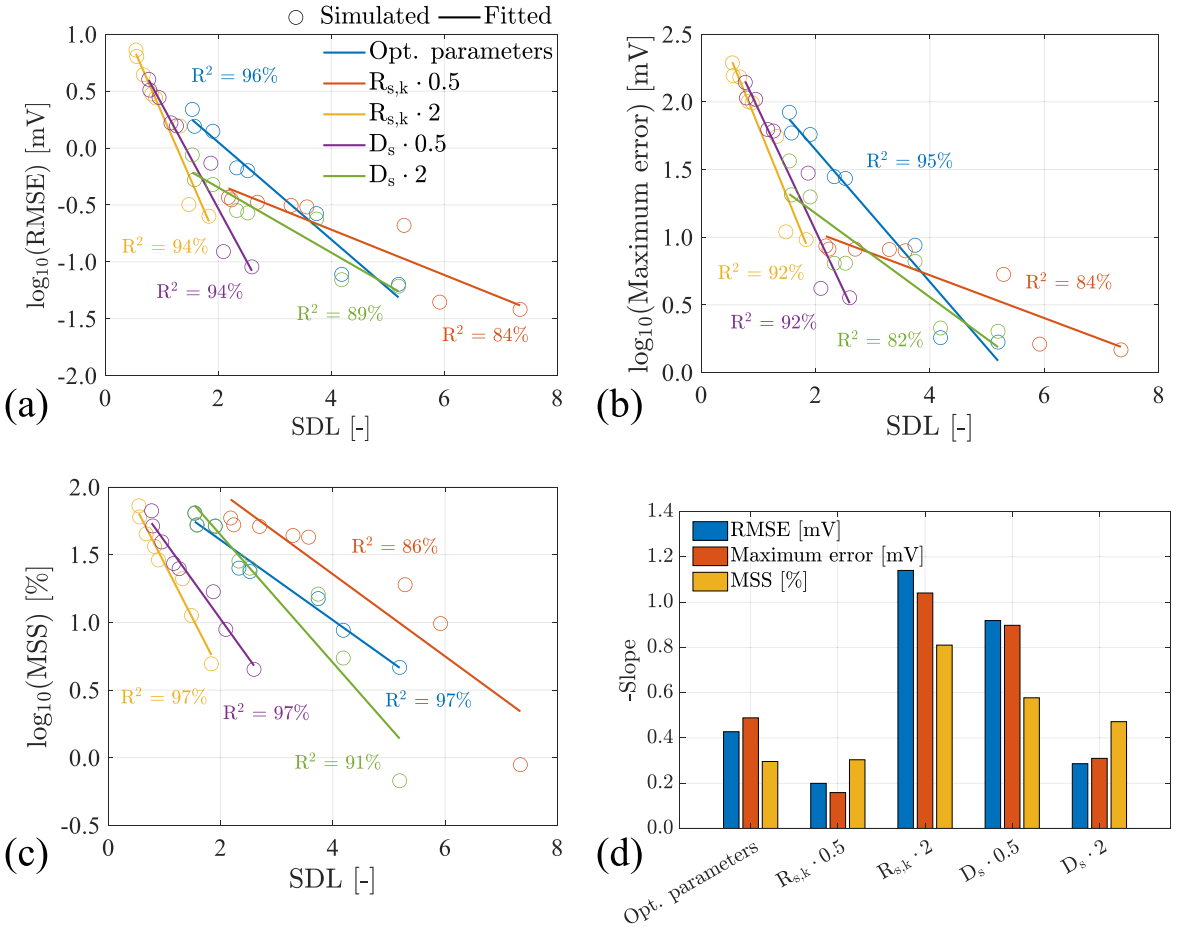

Figure 8. Simulation results (symbols) from the simplified MP-DFN and hybrid MP-DFN models compared with the MP-DFN reference model, with RMSE (a), maximum error (b), and MSS (c) as a function of SDL for different model parameter values ($R_{s,k}$ and D_s). Linear regression lines are indicated by the lines. Slopes of the linear regression lines as a function of the different parameter values (d). Note that the values on the y-axes of (a)-(c) are calculated using the base-10 logarithm.

an SDL of 2.64 and 1.35, respectively. The simplified MP-DFN model has with 2.2 mV the highest RMSE, as expected. In addition, it can be observed that the simplified MP-DFN model has the highest error at the beginning of charging with a maximum error of 83.5 mV, compared to 57.4 mV and 8.7 mV for the hybrid MP-DFN with SDL 1.35 and 2.64, respectively. The error during the WLTP cycle is magnified in the inset of Fig. 7b. The error comes from the nature of the approximation, which fails to provide accurate simulation results at rapid voltage changes.[30]

Figure 7c shows a comparison between the RMSE and MSS for the simplified MP-DFN model and hybrid MP-DFN models with SDL values of 1.35 and 2.64. MSS improvements relative to the MP-DFN model of 28%, 66%, and 69% are achieved when using an SDL of 2.64, 1.35, or the simplified MP-DFN model, respectively. Figure 7c additionally shows simulations of the hybrid MP-DFN model with SDL values of 1.78 and 1.09 (grey symbols) for comparison purposes. When looking at all symbols in Fig. 7c, a clear exponential increase in RMSE as a function of MSS can be observed, as illustrated by the dashed fitted line. The MSS improvement can be traced back to the difference in the number of nodes to be solved by FDM, as illustrated in Fig. 7d. The MP-DFN uses a total of 7980 nodes in the solid region of the two electrodes (Table III) to solve Eq. 1. In comparison, the hybrid MP-DFN with SDL 2.64 and 1.35 use 5027 and 2074 nodes, respectively. The simplified MP-DFN model only uses 260 nodes to be solved by FDM, making it the fastest to calculate and significantly reducing the amount of stored data.

Sensitivity analysis.—In this sensitivity analysis, the effects of parameter variations on the model simulations are studied. Specifically, $R_{s,k}$ and D_s were increased and decreased by a factor of two during a 5C-rate charging process followed by the WLTP cycle. The optimized number of nodes and the SDL based on particle ranking are shown in Tables S1 and S2, respectively. These parameter adjustments represent the changes that would occur when using an electrode with a different particle size distribution or when operating at a different temperature, which significantly influences D_s. Figures 8a–8c show the results for RMSE, maximum error, and MSS, respectively. The sensitivity analysis indicates that the results are strongly dependent on the modified parameters. Multiplying $R_{s,k}$ by a factor of 2 results in the highest RMSE, maximum error, and MSS across various SDLs. This is followed by multiplying D_s by a factor of 0.5, multiplying D_s by a factor of 2, and lastly, multiplying $R_{s,k}$ by a factor of 0.5. When performing simulations on electrodes with large particle sizes and/or low diffusion coefficients, it is advised to select relatively high SDL values in order to keep errors low. However, this is user specific and therefore choosing a suitable SDL achieves the required balance between accuracy and computational speed with the hybrid MP-DFN model.

The slopes of the fitted linear regression lines from Figs. 8a–8c are calculated and shown in Fig. 8d. The lowest slopes correspond to $R_{s,k}$ multiplied by a factor of 0.5, and the highest slopes correspond to $R_{s,k}$ multiplied by a factor of 2. As mentioned in the elaboration on Fig. 6d, a lower slope is a result of a smaller difference between minimum and maximum SDL, whereas a

higher slope is a result of a larger difference. The differences in slope with respect to the optimized parameter set directly indicate the parameter sensitivity. That means that a large difference in slope to the optimized parameter set has a high impact on the model's KPI. Specifically, increasing $R_{s,k}$ results in the highest deviations in RMSE, maximum error, and MSS with respect to the optimized parameter set, indicating a high sensitivity. Conversely, changes in D_s show a relatively moderate impact on slope variations compared to changes in $R_{s,k}$. This becomes evident from Eq. 8, where D_s appears within the square root, and from Figs. 3a–3b, which shows greater SDL variations with changes in $R_{s,k}$ than in D_s. These findings underscore the importance of carefully selecting and tuning the optimum SDL based on the battery design and operational conditions.

Conclusions

This study introduces two novel models: the simplified MP-DFN model and the hybrid MP-DFN model. The simplified MP-DFN model is a simplified version of the MP-DFN model that utilizes Padé approximations for faster calculation times, addressing the computational challenges of the MP-DFN model, which uses the FDM method to calculate diffusion inside electrode particles. The hybrid MP-DFN model further advances this by combining Padé approximations and the FDM method for calculating diffusion. The hybrid MP-DFN model uses the SDL as an indicator to determine whether a particle should be solved with FDM or Padé approximation and, therefore, optimizes the balance between accuracy and computational speed. Selecting an optimum SDL is heavily dependent on model parameters and operational conditions, such as particle radii, diffusion constant, and C-rate. The hybrid MP-DFN model effectively bridges the gap between the high computational power required by the MP-DFN model and the approximation-based simplified MP-DFN model, resulting in improved accuracy with a slight compromise on computational speed. This dual-model approach is advantageous in various contexts, including generating simulation training data for machine learning approaches, simulating long-term aging, and its applicability for integration into battery management systems (BMS).

Acknowledgments

The authors thank their colleagues at Forschungszentrum Jülich GmbH for their great support and especially acknowledge Dr Kudakwashe Chayambuka for his insightful discussions. This study has been developed in the LLEC::VxG and ALIBES projects, which are funded by the German Federal Ministry of Education and Research under Grant No. 03SF0628 and 13XP0530B, respectively.

List of symbols

Nomenclature

A_{surf}	Electrode surface area, m^2
$a_{s,k}$	Specific interfacial surface area of the kth particle, m^{-1}
b	Bruggeman coefficient, -
c_e	Concentration in the electrolyte phase, mol m^{-3}
$c_{e,0}$	Initial electrolyte concentration, mol m^{-3}
$c_{s,k}$	Concentration in the solid phase of the kth particle, mol m^{-3}
$c_{s,k}^{avg}$	Average concentration in the solid phase of the kth particle, mol m^{-3}
c_s^{max}	Maximum concentration in the solid phase of the kth particle, mol m^{-3}
$c_{s,k}^{surf}$	Surface concentration in the solid phase of the kth particle, mol m^{-3}
D_e	Diffusion coefficient in electrolyte phase, m^2s^{-1}
D_s	Diffusion coefficient in the solid phase, m^2s^{-1}
F	Faraday constant, 96487 C mol^{-1}
f_k	Fraction of kth particle of the total number of particles, -
$f_\pm$	Mean molar activity coefficient of the electrolyte, -
$i_{0,k}$	Exchange current density of the kth particle, A m^{-2}
I_{app}	Applied current, A
$j_{Li,k}$	Molar ionic flux of the kth particle, mol $m^{-2}s^{-1}$
k	Number of particles
k_0	Reaction-rate constant, $mol^{5/2}m^{-1/2}s^{-1}$
L	Overall thickness of the cell, m
m	Number of C-rates
N	Number of selected particle radii
R	universal gas constant, 8.314 J $mol^{-1}K^{-1}$
r	Radial position across a spherical particle, m
R_{cc}	Contact resistance, $\Omega\ m^2$
$R_{s,k}$	Radius of the kth particle, m
R_f	Film resistance, $\Omega\ m^2$
s	Frequency domain, -
T	Temperature, K
t	Time, s
t_+^0	Transference number, -
t_f	Simulation time of the reference model, s
t_s	Simulation time of the simplified models, s
U_k	Equilibrium potential of the electrode of the kth particle, V
V_{cell}	Battery output voltage, V
x	Position across cell layers, m

Greek

α_a	Anodic charge-transfer coefficients, -
α_c	Cathodic charge-transfer coefficients, -
δ	Thickness, m
ε_e	Electrolyte volume fraction, -
ε_s	Active material volume fraction, -
η_k	Electrode overpotential of the kth particle, V
$\hat{\theta}$	Optimized set of parameters
θ	Unoptimized set of parameters
κ_e	Ionic conductivity, S m^{-1}
ν	Thermodynamic factor, -
σ_s	Solid phase electronic conductivity, S m^{-1}
ϕ_e	Electrolyte phase potential, V
ϕ_s	Solid-phase potential, V
χ	Stoichiometry, -

ORCID

Haider Adel Ali Ali https://orcid.org/0009-0003-6923-8957
Luc H. J. Raijmakers https://orcid.org/0000-0002-7166-8644
Hermann Tempel https://orcid.org/0000-0002-9794-6403
Dmitri L. Danilov https://orcid.org/0000-0003-2980-059X
Peter H. L. Notten https://orcid.org/0000-0003-4907-8426
Rüdiger-A. Eichel https://orcid.org/0000-0002-0013-6325

References

1. J. W. Choi and D. Aurbach, *Nat Rev Mater*, **1**, 1 (2016).
2. C. Pillot, *The rechargeable battery market and main trends 2018–2030*, *36th annual international battery seminar & exhibit. avicenne energy* (2019).
3. I. Tsiropoulos, D. Tarvydas, and N. Lebedeva, *Li-ion batteries for mobility and stationary storage applications*, *EUR 29440 EN*, Publications Office of the European Union, Luxembourg (2018), JRC113360.
4. J. Newman and N. P. Balsara, *Electrochemical Systems* (Wiley, New York) (2021).
5. M. Doyle, T. F. Fuller, and J. Newman, *J. Electrochem. Soc.*, **140**, 1526 (1993).
6. Z. Chen, D. L. Danilov, R-A. Eichel, and P. H. L. Notten, *Adv. Energy Mater.*, **12**, 2201506 (2022).
7. C. Zou, A. G. Kallapur, C. Manzie, and D. Nešić, *2015 54th IEEE Conference on Decision and Control (CDC)*1328 (2015).
8. R. Klein et al., *Proceedings of the 2011 American Control Conference*382 (2011).
9. T. L. Kirk, J. Evans, C. P. Please, and S. J. Chapman, *SIAM J. Appl. Math.*, **82**, 625 (2022).
10. F. B. Planella et al., *Prog. Energy*, **4**, 042003 (2022).
11. P. Mohtat, S. Lee, V. Sulzer, J. B. Siegel, and A. G. Stefanopoulou, *J. Electrochem. Soc.*, **167**, 110561 (2020).
12. V. Srinivasan and J. Newman, *J. Electrochem. Soc.*, **151**, A1517 (2004).
13. M. Farkhondeh and C. Delacourt, *J. Electrochem. Soc.*, **159**, A177 (2011).

14. Z. Mao, M. Farkhondeh, M. Pritzker, M. Fowler, and Z. Chen, *J. Electrochem. Soc.*, **163**, A458 (2015).
15. T. L. Kirk, C. P. Please, and S. J. Chapman, *J. Electrochem. Soc.*, **168**, 060554 (2021).
16. M. M. Majdabadi, S. Farhad, M. Farkhondeh, R. A. Fraser, and M. Fowler, *J. Power Sources*, **275**, 633 (2015).
17. M. Petit, E. Calas, and J. Bernard, *J. Power Sources*, **479**, 228766 (2020).
18. M. Torchio, L. Magni, R. B. Gopaluni, R. D. Braatz, and D. M. Raimondo, *J. Electrochem. Soc.*, **163**, A1192 (2016).
19. Z. Khalik, M. C. F. Donkers, and H. J. Bergveld, *J. Power Sources*, **488**, 229427 (2021).
20. V. R. Subramanian, V. D. Diwakar, and D. Tapriyal, *J. Electrochem. Soc.*, **152**, A2002 (2005).
21. L. Xia, E. Najafi, Z. Li, H. J. Bergveld, and M. C. F. Donkers, *Appl. Energy*, **208**, 1285 (2017).
22. T-S. Dao, C. P. Vyasarayani, and J. McPhee, *J. Power Sources*, **198**, 329 (2012).
23. Y. Li et al., *IEEE Ind. Electron. Mag.*, **16**, 36 (2022).
24. K. Liu et al., *Control Eng. Pract.*, **124**, 105176 (2022).
25. R. S. Thiagarajan et al., *J. Electrochem. Soc.*, **170**, 010528 (2023).
26. G. Fan, K. Pan, and M. Canova, *54th IEEE Conference on Decision and Control (CDC)* (IEEE, Osaka)3922 (2015), http://ieeexplore.ieee.org/document/7402829/.
27. N. T. Tran et al., *J. Electrochem. Soc.*, **165**, A1409 (2018).
28. Y. Shi, G. Prasad, Z. Shen, and C. D. Rahn, *Proceedings of the 2011 American Control Conference*356 (2011).
29. J. C. Forman, S. Bashash, J. L. Stein, and H. K. Fathy, *J. Electrochem. Soc.*, **158**, A93 (2010).
30. H. A. A. Ali et al., *Electrochim. Acta*, **493**, 144360 (2024).
31. Z. Deng, L. Yang, H. Deng, Y. Cai, and D. Li, *Energy*, **142**, 838 (2018).
32. X. Han, M. Ouyang, L. Lu, and J. Li, *J. Power Sources*, **278**, 802 (2015).
33. K. Chayambuka, G. Mulder, D. L. Danilov, and P. H. L. Notten, *Journal of Applied Mathematics and Physics*, **8**, 1066 (2020).
34. J. D'Errico, (2024), fminsearchbnd, fminsearchcon (https://www.mathworks.com/matlabcentral/fileexchange/8277-fminsearchbnd-fminsearchcon), MATLAB Central File Exchange. Retrieved November 20, 2024.
35. M. Shadman Rad, D. L. Danilov, M. Baghalha, M. Kazemeini, and P. H. L. Notten, *Electrochim. Acta*, **102**, 183 (2013).